RESEARCH ARTICLE

ADVANCED OPTICAL MATERIALS
www.advopticalmat.de

Ultrafast Shift Current in SnS_2 Single Crystals: Structure Considerations, Modeling, and THz Emission Spectroscopy

Kateryna Kushnir Friedman, Sepideh Khanmohammadi, Erin M. Morissette, Curtis W. Doiron, Roy Stoflet, Kristie J. Koski, Ronald L. Grimm, Ashwin Ramasubramaniam, and Lyubov V. Titova**

Above-band gap optical excitation of non-centrosymmetric semiconductors can lead to the spatial shift of the center of electron charge in a process known as shift current. Shift current is investigated in single-crystal SnS_2, a layered semiconductor with the band gap of ≈2.3 eV, by THz emission spectroscopy and first principles density functional theory (DFT). It is observed that normal incidence excitation with above gap (400 nm; 3.1 eV) pulses results in THz emission from 2H SnS_2 ($P\bar{3}m1$) polytype, where such emission is nominally forbidden by symmetry. It is argued that the underlying symmetry breaking arises due to the presence of stacking faults that are known to be ubiquitous in SnS_2 single crystals and construct a possible structural model of a stacking fault with symmetry properties consistent with the experimental observations. In addition to shift current, it is observed THz emission by optical rectification excited by below band gap (800 nm; 1.55 eV) pulses but it requires excitation fluence more than two orders of magnitude higher to produce same signal amplitude. These results suggest that ultrafast shift current in which can be excited with visible light in blue–green portion of the spectrum makes SnS_2 a promising source material for THz photonics.

1. Introduction

Above-gap photoexcitation of a non-centrosymmetric semiconductor where the real-space center of charge for the valence bands differs from that of the conduction bands can give rise to a shift current, a spatial charge transfer of the order of the bond length.[1–7] It is a second-order nonlinear optical effect that is governed by the same symmetry rules as optical rectification. While it is sometimes termed above-band-gap rectification, it is a distinctly different process: the shift current involves real carriers generated by interband excitation while optical rectification results from polarization of virtual carriers and occurs for all photon energies. With sub-picosecond duration of the optical excitation, both optical rectification and shift current can result in emission of electromagnetic pulses in the terahertz (THz) frequency range. For above-gap excitation, the shift current significantly outweighs the rectification current and is a dominant contribution to the second-order nonlinear response.[2,3,8]

Study of THz emission provides a view into the symmetry properties of materials and, in the case of above-gap excitation, into the nature and dynamics of ultrafast photoexcited current. Even when a material is nominally centrosymmetric, inversion symmetry breaking at the surface or at internal interfaces (e.g., grain boundaries and stacking faults) can result in second-order nonlinear responses allowing, for example, targeted investigation of the photocurrents that involve topological surface states in topological insulators Bi_2Se_3 and Bi_2Te_3.[9–12] Another class of materials where THz emission spectroscopy has been applied to probe nonlinear optical properties is transition-metal dichalcogenides (TMDs) of the formula MX_2, layered 2D semiconductors

K. Kushnir Friedman, S. Khanmohammadi, E. M. Morissette[+], L. V. Titova
Department of Physics
Worcester Polytechnic Institute
Worcester, MA 01609, USA
E-mail: kkushnir@wpi.edu; ltitova@wpi.edu

The ORCID identification number(s) for the author(s) of this article can be found under https://doi.org/10.1002/adom.202400244

[+]Present address: Department of Physics, Brown University, Providence, RI 02912, USA

[Correction added on April 27, 2024, after first online publication: The 8th Author's name was corrected as Ramasubramaniam.]

DOI: 10.1002/adom.202400244

C. W. Doiron, R. Stoflet, R. L. Grimm
Department of Chemistry and Biochemistry
Worcester Polytechnic Institute
Worcester, MA 01609, USA

K. J. Koski
Department of Chemistry
University of California
Davis, CA 95616, USA

A. Ramasubramaniam
Department of Mechanical and Industrial Engineering
University of Massachusetts
Amherst, MA 01003, USA

A. Ramasubramaniam
Graduate Program in Materials Science and Engineering
University of Massachusetts
Amherst, MA 01003, USA

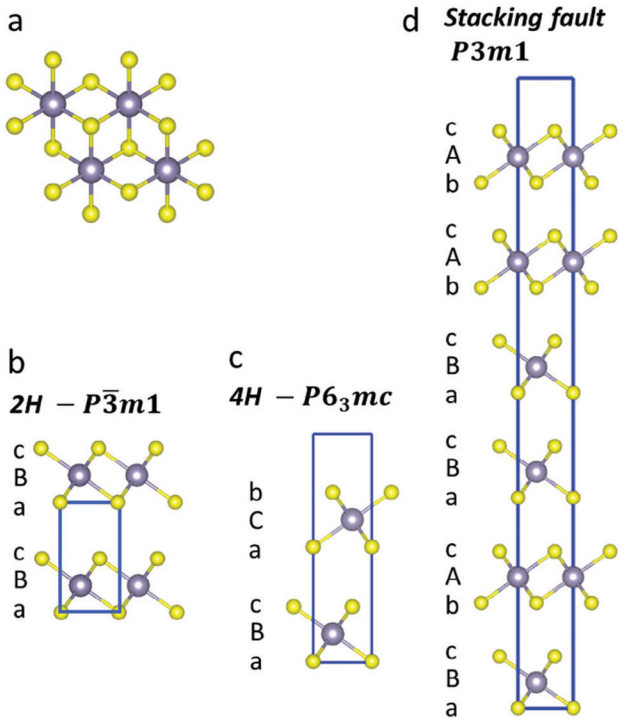

Figure 1. Structure of SnS_2: a) a top view of the basal plane; b,c) stacking sequences for 2H ($P\bar{3}m1$) and 4H ($P6_3mc$) polytypes; d) structural model of stacking faults with $P3m1$ symmetry. (Sn: grey spheres; S: yellow spheres).

with van der Waals (vdW) interactions between the layers.[13–17] In a prototypical TMD material, MoS_2, trigonal prismatic coordination exists between the Mo and S atoms. It does not have inversion symmetry in a monolayer form and exhibits second-order nonlinearities.[17–19] In a naturally found and most commonly observed phase of MoS_2, known as 2H-MoS_2, bulk inversion symmetry is restored by layer stacking and experimentally observed shift current response arises solely in the surface layer.[13–17] In other members of layered MX_2 TMDs, such as TiS_2 and $TiSe_2$, ZrS_2, VSe_2, and SnS_2, chalcogenide atoms in a single layer do not stack directly above one another but are staggered, resulting in octahedral rather than trigonal coordination.[18,20–22] In this case, monolayers possess inversion symmetry, ruling out second-order nonlinear effects such as the shift current or optical rectification. However, different possible stacking sequences in bulk single crystals of these MX_2 materials can produce different structures, or polymorphs, including those that are noncentrosymmetric.[23]

Here, we focus on SnS_2, an earth-abundant 2D layered TMD with a band gap in the visible range of spectrum (≈2.3 eV), good environmental stability and high carrier mobility, that has already attracted attention as a material for photo-electrochemistry and field effect transistors.[21,24–28] The SnS_2 multilayers can exist in different polytypes, characterized by distinct stacking sequences.[29–32] Most common polytypes are 2H and 4H (**Figure 1**) in the Ramsdell notation. It should be noted here that the accepted polytype nomenclature for MoS_2 and SnS_2 differ, and the structure designated as 2H for SnS_2 is known as 1T for MoS_2 and gives rise to metallic MoS_2.[33,34] In 2H SnS_2 (Figure 1b), a unit cell has two sulfur layers, and the stacking sequence is $[(aBc)]_n$ when viewed along [110] direction where lower case letters label S atoms, and capital letters label Sn atoms. This phase is characterized by $P\bar{3}m1$ space group (no. 164) which preserves inversion symmetry of the monolayer. Another common polytype, 4H (Figure 1c), is non-centrosymmetric and characterized by the $P6_3mc$ space group (no. 186).[35] In addition, 18R polytype has also been observed but it is centrosymmetric ($R\bar{3}m$ space group 166).[35]

The polytype composition in SnS_2 single crystals grown by chemical transport is determined by synthesis conditions, viz. growth temperature and the choice of transporting agent, although the exact phase diagram for formation of the different polytypes has not yet been established.[35–37] For different carrier agents such I_2 or SnI_4, growth at temperatures above 800 °C produces predominantly 4H SnS_2, while the crystals grown at low temperatures (< 600 °C) temperature tend to have 2H stacking.[35,37] In addition, when SnI_4 is used as a transporting agent, 18R polytype is frequently observed at intermediate temperatures (≈700 °C), but it is rare in crystals grown with I_2.[35] At intermediate temperatures, different polytypes can coexist, separated by strain-free stacking faults.[32,35] Stacking disorder and intergrown polytype domains have also been observed in other single crystalline TMDs such as MoS_2, $MoSe_2$, and WSe_2.[38–40]

Recent reports demonstrated THz emission in response to non-resonant, sub-gap excitation of single crystal SnS_2 and proposed optical rectification as the mechanism.[41,42] However, the relationship between nonlinear optical properties of SnS_2 and its crystal structure remains an open question. In this study, we report on THz emission in single crystalline SnS_2 excited at normal incidence with both above bandgap (400 nm) and below band gap (800 nm) laser pulses. While the symmetry properties of both effects is the same, resonant, above-gap excitation results in emission that is more than two orders of magnitude larger for similar excitation fluence, suggesting an ultrafast shift current as a source.[3] While the structural characterization of the sample reveals the centrosymmetric 2H polytype, the symmetry properties of the THz emission are consistent with those of the shift-current tensor for a non-centrosymmetric P3m1 structure, as confirmed from first principles density functional theory (DFT). We argue that the presence of stacking faults that are known to be ubiquitous in SnS_2 crystals results in local breaking of the inversion symmetry that gives rise to the ultrafast shift current in the basal plane of SnS_2 layers and construct a possible structural model of stacking faults that can have symmetry properties matching experimental observations (Figure 1d). These findings highlight the capability of THz emission spectroscopy to detect disorder in single crystals. They also suggest that above-gap excitation of SnS_2 in blue–green visible range is promising for efficient, ultrathin shift-current THz emitters as well as for shift-current photovoltaic devices.[43]

2. Experimental Results

2.1. SnS_2 Structure

Two-zone chemical vapor transport as in **Figure 2a** yielded single-crystal SnS_2 flakes that were 1–10 mm wide and several microns thick. Annotated peaks in a characteristic X-ray diffraction (XRD) spectrum (Figure 2c) align with known features that support the

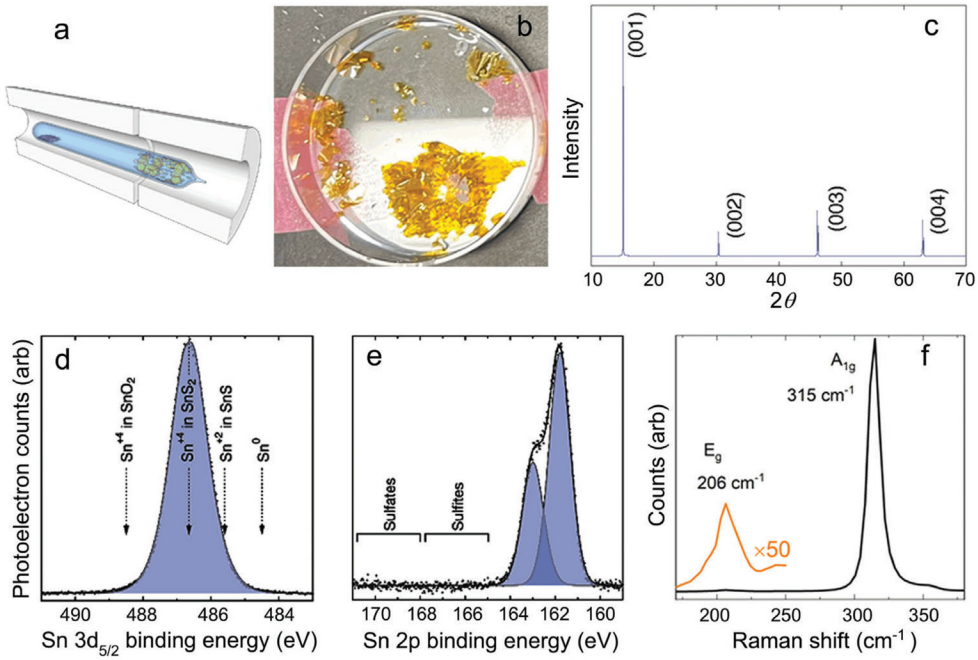

Figure 2. a) Schematic of CVT growth. b) Resulting SnS_2 single crystals. c) XRD diffraction. XPS spectra in d) Sn $3d_{5/2}$ region and e) S 2p region. f) Raman scattering spectrum.

synthesis of phase-pure SnS_2 with no deleterious contributions from polymorphs such as SnS or Sn_2S_3. Single crystal diffraction identified the crystals as the 2H phase (space group $P\bar{3}m1$) with lattice constants a = 3.6466(10) Å, b = 3.65466(10) Å, c = 5.890(2) Å, and $\alpha = 90°$ $\beta = 90°$, $\gamma = 120°$. This is confirmed by Rietveld refinement of powder X-ray diffraction data (Figure 2c) using MAUD,[44] which finds a = 3.63(1) Å and c = 5.894(1) Å. Peak broadening, beyond instrumental linewidth broadening, in the powder XRD is consistent with defects such as stacking faults.[45–47] The presence of stacking faults is apparent in XRD both from peak shifts and more from peak broadening.[45–47] SnS_2 is well-known to be susceptible to stacking faults, like most van der Waals materials.[48] To determine the average crystallite thickness within each stacking fault, we can perform a Debye–Scherrer analysis similar to analysis by Anitha et al.[47] specifically on the (00l) peaks which corresponds to the d-spacings in the stacking direction. The crystals themselves are thick, with thicknesses on the order of microns to tens of microns (Figure 2b). The average crystallite thickness from XRD, which is approximately the average stacking fault thickness, was calculated as 93–121 nm from two single crystal samples using the (00l) peaks and from the Debye–Scherrer formula (Eq 1) after stripping the XRD powder pattern of the kα_2 contribution.[45]

$$D = \frac{\kappa \lambda}{\beta \cos\theta} \tag{1}$$

where κ is the shape factor (0.94), λ is the wavelength of the Cu kα source (λ = 1.54178 Å), θ is the Bragg angle, and β is the full width at half maximum value calculated considering the intrinsic linewidth of the XRD instrument determined from a NIST calibration sample of lanthanum hexaboride. A thickness of 93–121 nm from the XRD from crystals that are clearly microns thick suggests stacking faults with an average spacing of approximately 110 nm.

X-ray photoelectron spectroscopy (XPS) results support the synthesis of SnS_2. We ascribe a single feature centered at 486.6 eV in the Sn $3d_{5/2}$ region to modestly oxidized Sn^{+4} as expected for SnS_2 (Figure 2d) with no demonstrable contribution from highly oxidized Sn^{+4} attributable to SnO_2, from Sn^{+2} from SnS or Sn_2S_3, or from reduced Sn^0 metal. Features in the S 2p regions (Figure 2e) are well described by a single p-type doublet with no observable contributions from oxidized sulfur species at higher binding energies. XP spectra showed no interfacial iodine based on an absence of ascribable I 3d features. Notably, XP spectra of the O 1s region only demonstrated features with peaks between 533 and 531 eV that would be due to adventitiously adsorbed organics, rather than any Sn—O that we would expect to have a peak binding energy below 530 eV. In concert, the XRD and XPS results support the synthesis of high-purity SnS_2 with no interfacial oxidation.

Figure 2f shows a representative Raman spectrum of the single crystal SnS_2 material. Reports on the 2H and 4H polytypes elsewhere revealed subtle differences in Raman modes that can be used in polytype identification.[21,24,49] Specifically, while the spectra of both structures are dominated by a feature near 315 cm^{-1} (A_{1g} mode for 2H and a mixture of A_1 and E modes for 4H), weaker modes near ≈200 cm^{-1} differ between polytypes. The 2H polytype has a single E_g mode at 205 cm^{-1} while the 4H polytype exhibits a doublet at 200 and 214 cm^{-1} due to the E-mode.[21,24,49] In our case, we see a rather broad feature centered at 206 cm^{-1} and extending from 185 to 220 cm^{-1}. While it suggests that the 2H phase is the dominant contribution, broadening of the peak linewidth is consistent with stacking faults that are known to occur in SnS_2 or from anharmonic effects.[24,35,50] In addition, Brillouin scattering spectra are presented in Supporting Information

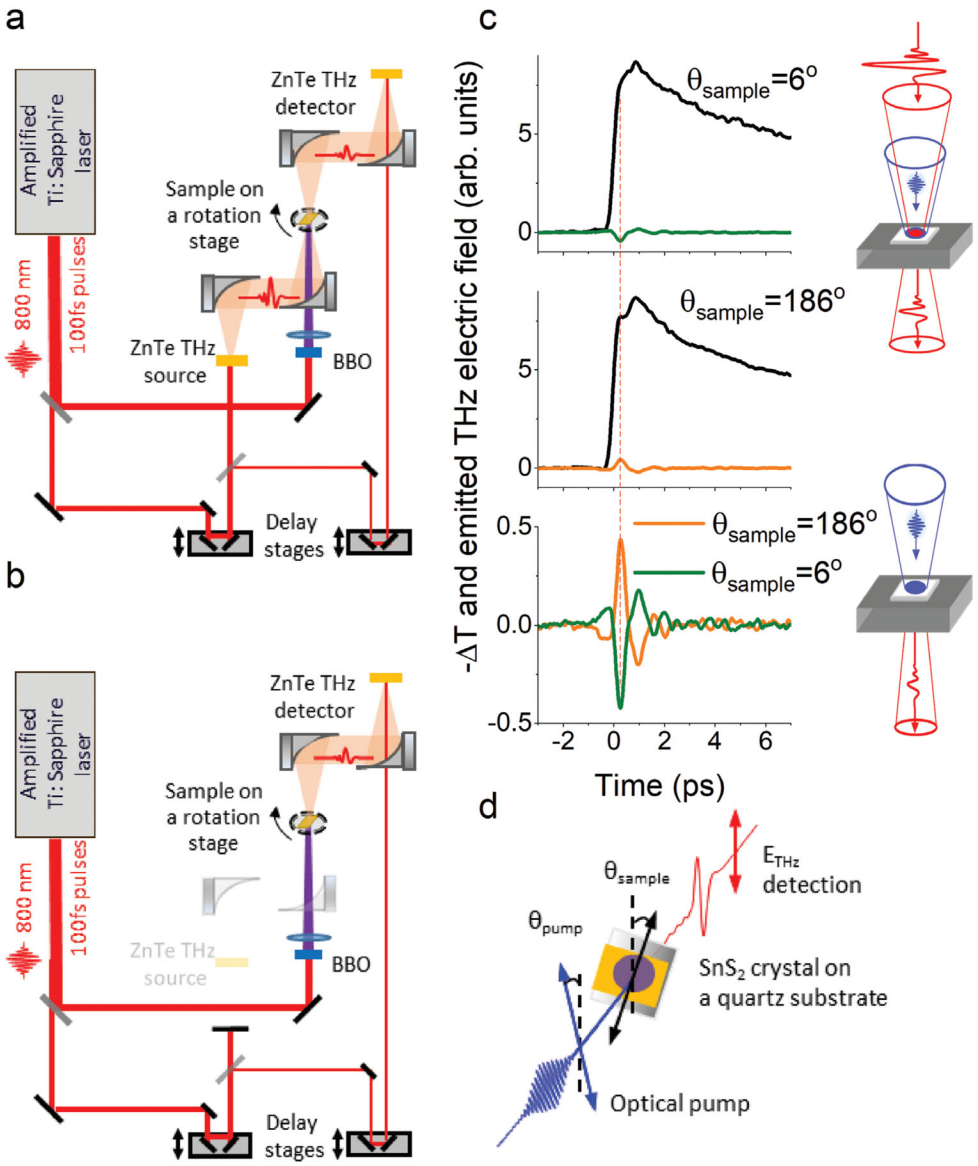

Figure 3. Schematics of a) TRTS and b) TES experiments. c) Example TRTS and TES data, collected for the 400 nm, 110 μJ cm^{-2} pump beam polarized along the THz detection (θ_{pump}=0°) and two different sample orientations, with the angles defined in (d).

which show spectral rotation symmetry consistent with a hexagonal phase of SnS_2 and identify a set of strong peaks that likely originate from the significant reflections resulting from defects and stacking faults.

2.2. Time-Resolved THz Spectroscopy

Photoexcitation with above-gap (400 nm) optical pulses injects free charge carriers, as time-resolved THz spectroscopy (TRTS) demonstrates in **Figure 3**. Figure 3a illustrates the TRTS experiment, in which SnS_2 crystal is excited at normal incidence with 400 nm, 100 fs pulses, and the resulting changes in conductivity are interrogated by time-delayed THz pulses in transmission geometry. Probe THz pulses have spectral bandwidth spanning 0.25–2.5 THz (1–10 meV) and are strongly absorbed by the free charge carriers present in the sample. Analysis of the changes to the transmitted THz pulses in response to the photoexcitation yields information on transient photoconductivity.[51] If the photoexcited sample itself is a source of THz emission, the signal reaching THz detector contains both the probe THz pulses generated in ZnTe source as well as those generated in the sample. It is possible to isolate THz emission in the sample by blocking the THz probe beam, effectively converting TRTS experiment to THz emission spectroscopy (TES), as shown in Figure 3b. The example traces of the changes in transmission of the THz probe pulse peak as a function of delay between the pump and the probe pulses for two different orientations of SnS_2 crystal are shown in Figure 3c (black curves). Same graphs also show THz emission by the sample itself for a particular sample orientation. THz emission occurs at the same time as photoconductivity increases in response to photoexcitation. The bottom graph in 3c shows that

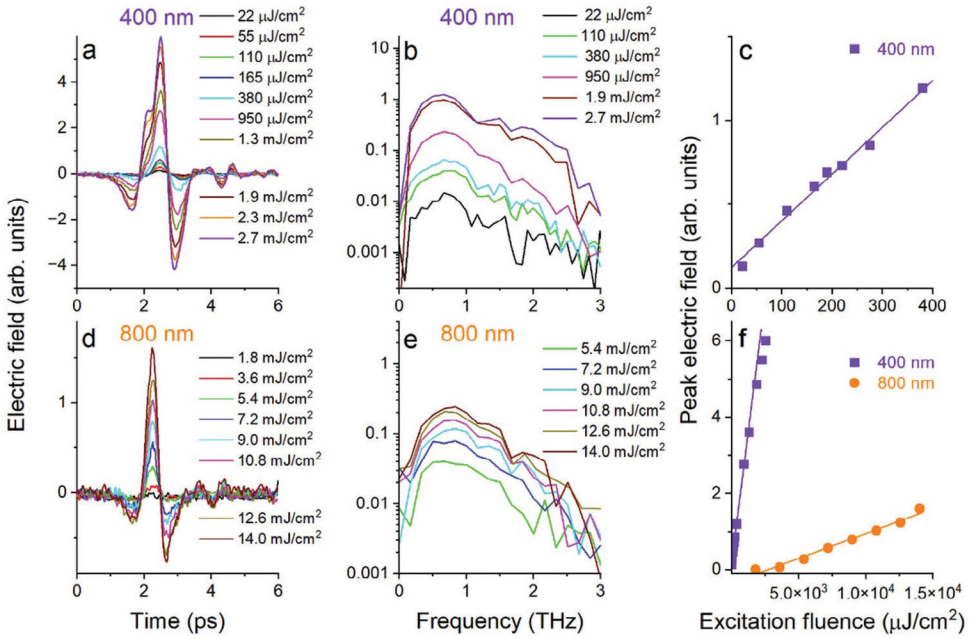

Figure 4. a) THz waveforms emitted by the SnS_2 crystal in response to photoexcitation with 400 nm, 100 fs pulses with the fluence indicated in the legend. The excitation beam is polarized along the THz detection axis (θ_{pump} =0°). The corresponding amplitude spectra at selected pump fluence values are shown in (b). c) Peak THz electric field as a function of fluence up to 400 μJ cm^{-2}. d) THz waveforms emitted by the same SnS_2 crystal in response to photoexcitation with 800 nm, 100 fs pulses with the fluence indicated in the legend. The corresponding amplitude spectra at selected pump fluence values are shown in (e). f) Peak THz electric field for 400 nm excitation and for 800 nm excitation as a function of fluence. Symbols in (c,f) represent experimental data, and the solid lines–linear fits to the data up to 400 μJ cm^{-2} range for 400 nm, and in the full studied range for 800 nm.

the THz waveforms emitted by SnS_2 change polarity when the sample is rotated by 180°, as will be discussed in detail later. In the TES experiment, detected THz emission component is defined by the orientation of ZnTe detector crystal as well as by the wire-grid polarizer placed before it and is fixed, but the sample orientation and the linear polarization of the excitation beam can be controlled independently, the former by rotation the sample on the sample stage, and the latter by rotating a half-wave plate placed in the beam (Figure 3d).

TRTS can characterize transient photoconductivity dynamics in SnS_2 following 400 nm excitation (Figure S1, Supporting Information). We find that excitation results in injection of free carriers that eventually get trapped at defect states and recombine over tens of picoseconds time scales, regardless of sample orientation relative to the THz probe pulse polarization. We also find that after the initial several picoseconds when both the THz probe pulse and THz emission from the sample co-propagate, charge carrier behavior is well described by the Drude model for free, non-interacting electron gas. The average carrier scattering time of 52 ± 2 fs and the effective mass value of $m^* = 0.375m_e$.[52] yield high mobility of 250 ± 10 cm^2 V^{-1} s^{-1}, in close agreement to prior reports, and provide further evidence that SnS_2 is highly crystalline.[24,25]

2.3. THz Emission Spectroscopy

As above bandgap excitation with 400 nm (3.1 eV) laser pulses with 110 μJ cm^{-2} fluence at normal incidence results in emission of THz pulses (Figure 3), and prior studies have uncovered similar emission with below band gap (800 nm) excitation at much higher (>1.2 mJ cm^{-2}) fluence,[41,42] we present THz emission properties of SnS_2 single crystal excited with both 800 nm and 400 nm with excitation fluences varying over the large range (22 μJ cm^{-2}–14 mJ cm^{-2}) in **Figure 4**. While 400 nm excitation results in THz emission at fluence as low as 22 μJ cm^{-2} (Figure 4a,b), two orders of magnitude higher excitation fluence is needed to observe the onset of THz emission under non-resonant, 800 nm, excitation (Figure 4d,e). The bandwidth of the observed emission extends to ≈3 THz for both excitation wavelengths, with emission peaked at 0.6 THz and FWHM of 0.7 THz. The bandwidth is independent of the excitation fluence for 800 nm and up to ≈1.3 mJ cm^{-2} for 400 nm. For 400 nm, temporal shape of the emitted pulse slightly changes as higher frequency contribution (>1.5 THz) increases at high fluences, possibly owing to the nonlinear effects of order higher than 2. The spectral bandwidth of the 1 mm thick ZnTe detector crystal (< 3THz) limits our ability to rigorously reconstruct the temporal behavior of the phenomena responsible for the THz emission, which requires a detector with the bandwidth exceeding the true spectral bandwidth of the emitted radiation.[53] We can nonetheless investigate symmetry and excitation fluence-dependent properties of THz generation. Fluence dependence of the peak of the emitted THz waveform is presented in Figure 4c,f. The peak of the emitted THz waveform can be fit to a linear function for 800 nm excitation over the entire studied fluence range, and for 400 nm at fluences < 500 μJ cm^{-2}. Sub-linear behavior of the emitted waveform peak at higher fluence values might also indicate higher-order response or can result from attenuation of transmitted THz pulses by high density of photogenerated

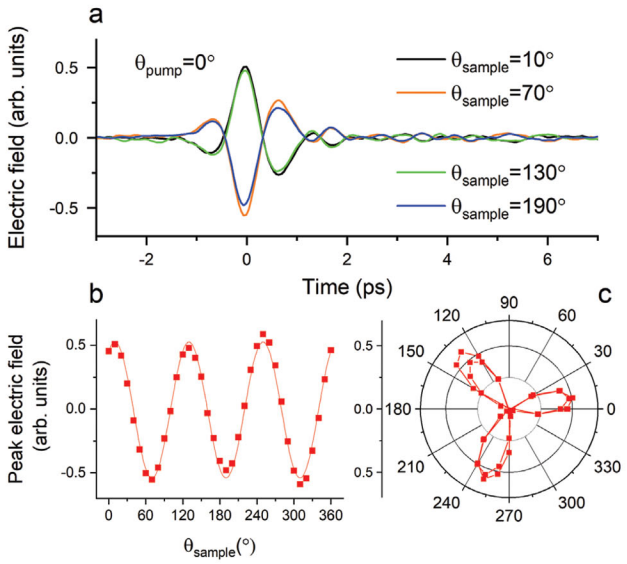

Figure 5. Dependence of THz emission from SnS_2 crystal following optical excitation with 400 nm, 220 μJ cm^{-2} pulses, linearly polarized along THz detection direction ($\theta_{pump} = 0°$), on sample orientation. a) Waveforms at four different orientations, b) peak electric field as a function of θ_{sample}, and the corresponding polar plot of emission amplitude (c). In (b), points are experimental data and the dashed line is the fit of the experimental data to $E_{peak}(\theta_{sample}) = E_0 cos(3\theta_{sample} - \theta_{0,sample})$.

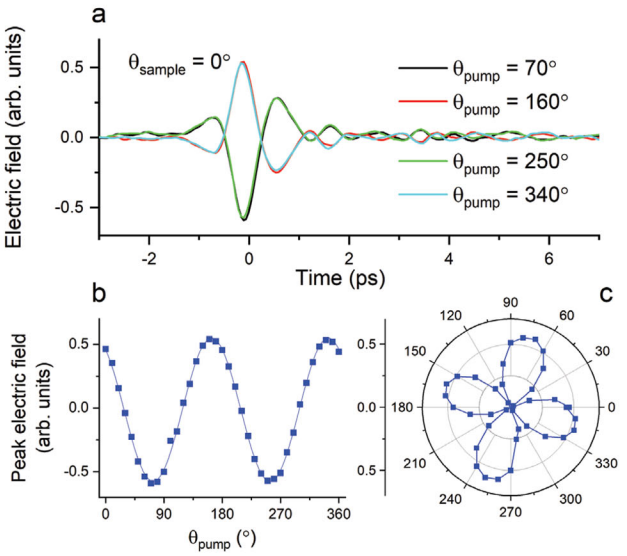

Figure 6. Dependence of THz emission from SnS_2 crystal following optical excitation with 400 nm, 220 μJ cm^{-2} pulses on the direction of the pump linear polarization ($\theta_{pump} = 0°$), with the sample orientation fixed at $\theta_{sample} = 0°$. a) Waveforms at four pump polarizations, b) peak electric field as a function of θ_{sample}, and the corresponding polar plot of emission amplitude (c). In (b), points are experimental data, and the dashed line is the fit of the experimental data to $E_{peak}(\theta_{pump}) = E_0 cos(2\theta_{pump} - \theta_{0,pump})$.

charge carriers as reported earlier in aligned carbon nanotube arrays[54] and in photoconductive THz sources.[55–57]

We have examined multiple crystals from different growth runs, and find that their properties viz. THz emission, its bandwidth and symmetry properties are the same (Figure S2, Supporting Information).

The symmetry properties of the observed THz emission in response to 400 nm excitation are examined in **Figure 5**. We find that the polarity of the emitted waveforms reverses every 60°, and as a result the waveform shape, including polarity, is fully reproduced every 120°. Plotting the peak of THz pulse as a function of sample orientation (θ_{sample}), we find that it fits well to $E_{peak}(\theta_{sample}) = E_0 \cos(3\theta_{sample} - \theta_{0,sample})$, where $\theta_{0,sample} = 6 \pm 1°$ is the offset between the high symmetry axis in the crystal and the THz detection axis (Figure 3d). Non-resonant excitation at 800 nm has the same symmetry properties (Figure S3, Supporting Information).

We also find that the emission depends on the linear polarization of the excitation, as shown in **Figure 6** for the sample orientation set to $\theta_{sample} = 0°$. Here, we find that the polarity of emission changes when the polarization of the excitation is rotated by 90°. The dependence of the peak of the electric field can on pump polarization can be described by $E_{peak}(\theta_{pump}) = E_0 \cos(2\theta_{pump} - \theta_{0,pump})$, with $\theta_{0,pump} = -20 \pm 5°$.

3. Discussion and DFT Modeling

Experimental data unambiguously show that excitation of single crystal SnS_2 with both above band gap, 400 nm, or below band gap, 800 nm, pulses, results in THz emission. With the linearly polarized excitation and detection at normal incidence (Figure 3) we can only detect THz emission due to the real or polarization currents parallel to the crystal surface, ruling out photo-Dember effect, photon drag, or emission due to drift of photoexcited carriers in built-in fields that are normal to the surface.[7,58–61] In the absence of an external in-plane bias, we have to consider second-order nonlinear processes as possible mechanisms behind the observed THz emission. A single color, linearly polarized excitation precludes injection current.[62] As the excitation fluence study (Figure 4) reveals, above-gap excitation with 400 nm pulses results in THz emission at fluence as low as 22 μJ cm^{-2}, while a two orders of magnitude higher excitation fluence is needed to observe the onset of THz emission under non-resonant, 800 nm, excitation, in good agreement with prior reports.[42] Emission in response to 800 and 400 nm excitation share the same symmetry properties under crystal rotation (Figure S3, Supporting Information), leading us to conclude that optical rectification is responsible for non-resonant THz excitation, while the shift current provides a dominant contribution to THz generation in response to above-gap excitation. At the same time, both of those second-order effects are precluded by the inversion symmetry of 2H of SnS_2, leaving the possibility of symmetry breaking by defects such as stacking faults as a plausible explanation.

Additional insight into the observed THz emission can be obtained via first principles DFT calculations. As shift current results in THz emission at much lower excitation fluences compared to optical rectification, and it therefore a more promising avenue for development of THz photonic devices under visible excitation. Thus, we focus on shift current in DFT modeling, noting again that the two effects share symmetry properties. As noted before, the 2H phase ($P\bar{3}m1$; space group 164) is centrosymmetric, which precludes a shift-current response. The 4H phase ($P6_3mc$; space group 186)[31] lacks centrosymmetry and may be considered as a possible candidate. With reference

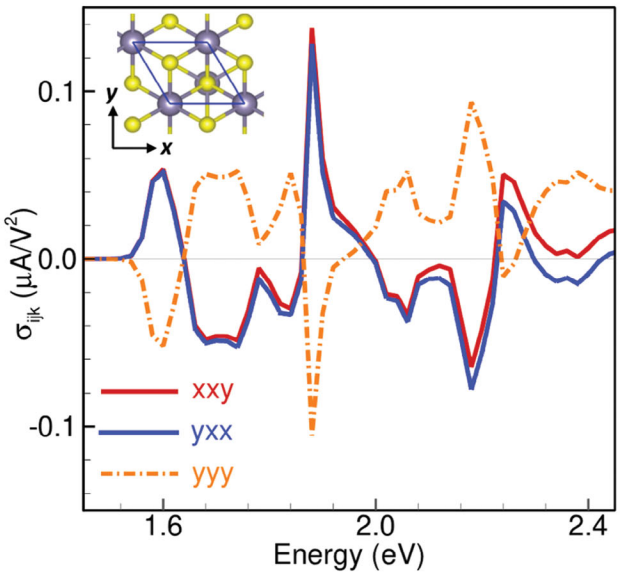

Figure 7. Shift-current tensor components of the stacking fault structural model shown in Figure 1d (space group 156; P3m1) calculated using density functional theory. A top view of the basal plane and the choice of Cartesian axes is indicated in the inset. Only those tensor components that contribute to the in-plane shift current (J_x, J_y) under normal incidence are displayed here.

to the Cartesian coordinate system indicated in **Figure 7**, the independent, non-zero components of the shift-current tensors for the $P6_3mc$ (space group 186) are (in Voigt notation)[63] $\sigma_{xxz} = \sigma_{yyz}$; $\sigma_{zxx} = \sigma_{zyy}$; σ_{zzz}. The shift current is given in component form as $J_i = \sigma_{ijk} E_j E_k$ ($i, j, k = x, y, z$; sum implied) from which it is clear that for a pump pulse polarized in the basal (x–y) plane of the crystal, as is the case in the experiments reported here (Figure 3d), the $P6_3mc$ phase will only have an out-of-plane (J_z) response that is not detectable in the experimental setup. The in-plane components (J_x and J_y) of the shift-current that would lead to the detected THz emission are identically zero. The same arguments apply for the crystal-air interface at the surface, where only the out-of-plane response J_z is possible Thus, we are led to consider the possibility of stacking faults that break inversion symmetry of the 2H phase locally being the cause for THz emission excited at the normal incidence.

Given the observed symmetries of the experimental signal, we constructed a structural model with stacking faults (Figure 1d) that displays overall P3m1 symmetry. For the $P3m1$ phase, the non-zero components of the shift-current tensor are[63] $\sigma_{xxy} = \sigma_{yxx} = -\sigma_{yyy}$; $\sigma_{xxz} = \sigma_{yyz}$; $\sigma_{zxx} = \sigma_{zyy}$; σ_{zzz}.[63] The in-plane components of the shift currents are then $J_x = 2\sigma_{xxy} E_x E_y$ and $J_y = \sigma_{yxx} E_x^2 + \sigma_{yyy} E_y^2 = \sigma_{yxx}(E_x^2 - E_y^2)$. When the linear polarization of the pump pulse (θ_{pump}) is rotated, keeping the crystal orientation (θ_{sample}) and the detection direction (E_{THz} direction in Figure 3d) probe fixed, $J_x = \sigma_0 E_0^2 \sin(2\theta_{pump})$ and $J_y = \sigma_0 E_0^2 \cos(2\theta_{pump})$, θ being the angle between the pump polarization and the x-axis, and we have set $\sigma_{xxy} = \sigma_{yxx} = -\sigma_{yyy} = \sigma_0$. The measured THz electric field component along the detection direction is thus given by $E_{THz}(\theta_{pump}) \propto \cos(2\theta_{pump} - \theta_0)$, where θ_0 is an arbitrary offset relative to the crystallographic axes, and is fourfold symmetric, as observed in the experiments (Figure 6). On the other hand, when the pump polarization is fixed ($\theta_{pump} = const$) and the sample is rotated, the shift current component aligned with the detection direction is given by $J = J_x \cos\theta' + J_y \sin\theta' = \sigma_0 E_0^2 \sin(2\theta + \theta')$, where θ is the angle between the pump polarization and the x-axis and θ' is that between the x-axis and detection direction. It then follows that the THz electric field at the detector is $E_{THz}(\theta_{sample}) \propto \sin(3\theta - \theta_0)$, which is threefold symmetric, similar to that presented in Figure 5.

Figure 7 displays results from DFT calculations of the three tensor components, σ_{xxy}, σ_{yxx} and σ_{yyy} as a function of excitation energy for the $P3m1$ stacking-fault model (Figure 1d). The complete set of calculated shift-current tensor components for the stacking fault structural model is shown in Figure S5 (Supporting Information). As seen from these data, the tensor components satisfy the expected relation $\sigma_{xxy} = \sigma_{yxx} = -\sigma_{yyy}$, minor deviations being attributed to numerical symmetry breaking within the calculations. Note that the onset of the shift-current response is not quantitatively correct due to the well-known problem of underestimation of band gaps with semi-local functionals and can potentially be remedied by using more accurate exchange-correlation functionals.[64,65] Specifically, the (indirect) DFT band-gap is ≈1.30 eV while the smallest direct gap (relevant to vertical transitions) is ≈1.56 eV, which is close to the observed onset of the shift-current response in Figure 7. In experiments, the excitation (400 nm) is approximately 0.6 eV above the actual band gap and so, in Figure 7, we have restricted attention to excitations that are up to 1 eV above the DFT band gap. Irrespective of the underestimation of the band gap in DFT, the results are qualitatively correct and consistent with the underlying space-group symmetries of the stacking-fault model.

While we have not examined a host of different stacking faults here, our model nevertheless gives credence to the hypothesis that stacking faults could indeed be the cause of the observed THz emission. We also recall here that changes in the stacking order can break inversion symmetry and result in large second-order nonlinearities such as second harmonic generation (SHG) in materials where the monolayers as well as the dominant polytypes of multilayer crystals are centrosymmetric, such as graphene trilayers.[66] Likewise, spontaneous incorporation of stacking faults in centrosymmetrically-stacked bulk layered structures of non-centrosymmetric monolayers, such as in the case of GeSe or $GeSe_{1-x}S_x$, can result in SHG at the stacking fault locations.[67] In our case, single crystal XRD analysis of crystals that have thickness on the order of microns to tens of microns suggested the presence of stacking faults with an average spacing of approximately 110 nm. Peak broadening in powder XRD, along with broadening of the E_g Raman mode at 206 cm^{-1}, and the appearance of an additional set of strong peaks is seen in the Brillouin scattering spectra (Figure S4, Supporting Information) and that is likely caused by the significant reflections resulting from defects and stacking faults, also all indirectly supporting the presence of stacking disorder. In the normal incidence geometry, stacking faults that produce the same local symmetry as the $P3m1$ phase of 4H polytype, which is the only phase that has non-zero in-plane shift current tensor elements, are responsible for the observed THz emission signal. With the absorption coefficient ≈10^5 cm^{-1} in single crystal SnS_2 at 400 nm,[68] the excitation pulse is mostly absorbed in ≈100 nm top layer and we conclude that the emitted THz radiation may originate from a

single stacking fault within the top-most layer of the single crystal. In this case, crystals with sub-micron thickness can be used as ultrathin THz emitters.

To summarize, our experiments reveal that the single crystalline SnS_2 with dominant 2H polytype structure exhibits a second-order nonlinear effect, a shift current, that has symmetry properties consistent with the *P*3*m*1 phase. To resolve this seemingly intractable contradiction, we hypothesize that the stacking disorder, where strain-free stacking faults that interrupt regions of 2H polytype, break inversion symmetry, giving rise to shift currents in the layers that form the faults. Observation of robust THz emission in this case underscores that THz emission spectroscopy is a sensitive tool of crystal structure and symmetry, able to detect localized symmetry breaking in single crystals even when bulk measurements such as XRD or Raman spectroscopy lack the sensitivity. This work also highlights the possible applications of SnS_2, an environmentally-stable 2D semiconductor that can be easily exfoliated to produce ultrathin crystals, in THz photonics.

4. Experimental Section

Sample Growth and Characterization: Chemical-vapor transport (CVT) yielded single-crystal SnS_2 as described earlier.[25] Quartz ampoules made from tubing (19 mm O.D., 17 mm I.D., G.M. Associates, Oakland, California) were sealed at one end, cleaned by a 1-week submersion in 10 w/v % $KOH_{(aq)}$, rinsed in 18 MΩ water, and oven dried at >100 °C until use. Loading under an air ambient included 1.3 g tin (99.999% purity, 1–3 mm pieces, Strem, Newburyport, Massachusetts, used as received), 0.75 g sulfur (resublimed ACS grade, 99.8%, Thermo Scientific, used as received), and 0.20 g molecular iodine (99.999% trace metal basis, Sigma–Aldrich, used as received). Upon loading, submersion of the bottom of the ampoule in an ice bath helped to lower the iodine vapor pressure and mitigate unwanted sublimation during the evacuation and sealing process. Tubes were evacuated through a connection to a diffusion-pump-equipped Schlenk line with a base pressure below 1×10^{-3} torr. Prompt sealing under vacuum yielded yield ≈22 cm ampoules with an iodine transport loading of approximately 4 mg mL^{-1}.

CVT syntheses utilized a two-zone tube furnace. Initially, growth runs utilized rapid heating to 800 °C at the newly sealed deposition side, and 2 °C min^{-1} heating to 700 °C in the "source" zone. Following a 6-h soak period of 700 °C in the source zone and 800 °C in the deposition zone, the temperature in the deposition zone decreased directly to and remained at 575 °C for 240 h whilst the source zone remained at 700 °C. Following this growth period, two successive cooling steps included one 6-h step of decreasing the temperature in the source zone at 2 °C min^{-1} to 300 °C while raising the temperature in the deposition zone at 2 °C min^{-1} to 600 °C, and a second cooling step to room temperature in both zones at a maximum rate of 2 °C min^{-1}.

XRD, XPS, and Raman spectroscopy characterized the resulting crystals. Single crystal XRD was acquired on a Bruker Smart APEX Duo with using a copper K-edge source (λ = 1.54178 Ang).

A Phi 5600 multitechnique instrument acquired XP spectra with a monochromated Al Kα anode sorce operating at 13.5 kV and 300 W. High resolution spectra for Sn 3d, S 2p, I 3d, O 1s, and C 1s regions utilized 25 meV steps at a 23.5 eV pass energy while wide-area survey spectra utilized 500 meV steps at a 117.4 eV pass energy. Data fitting utilized psedo-Voigt GL(*x*) fitting functions where *x* linearly varies between 0 for a pure Gaussian and 100 for a pure Lorentzian line shape. Fitting in the S 2p region utilized spin-orbit-split doublets with a splitting of 1.16 eV, mutually identical fwhm values, and an area ratio of 0.511 between the $2p_{1/2}$ and the $2p_{3/2}$ features.

Raman spectra of the samples were obtained using an XploRa Raman microscope (Horiba Scientific, USA) operating with a 532 nm laser. Laser light was focused on the sample using a 100× magnification lens from Olympus, and an 1800 groove/mm grating was used along with accumulation time of 2 s and 25 repetitions to collect the signal.

THz Spectroscopy: For TRTS, ultrashort (100 fs), 800 nm pulses from an amplified Ti: sapphire laser (Coherent Libra®) source were split into three beams. One was used to generate 400 nm pulses by the 2nd harmonic generation in a 0.5 mm thick BBO crystal, with conversion efficiency ≈15%. A short-pass filter was used to block the fundamental beam after the BBO. This beam was used to optically excite the sample. The other two beams, time-delayed with respect to the optical excitation beam by computer-controlled mechanical delay stages, were used to generate THz pulses in a 1 mm thick [110] ZnTe crystal by optical rectification and detect them in the second ZnTe crystal using electro-optic sampling. THz pulses were collected and focused using off-axis parabolic mirrors. The sample on a quartz substrate were placed onto a rotation stage in the focus of the THz beam. Measurements were carried out in transmission mode, at a normal incidence. An aperture with 1.5 mm diameter placed in front of the sample ensured that the THz beam probed the uniformly illuminated central portion of the larger diameter (5 mm) excitation beam.

For TES, the THz probe beam in TRTS setup was blocked, while the excitation beam was focused onto the sample in the same way as it is done in TRTS. Detected component of THz emission by the sample was fixed, defined by the orientation of ZnTe detector crystal and by the wire-grid polarizer placed before it. The sample orientation was controlled by rotation of the sample by a computer-controlled sample stage. The linear polarization of the excitation beam was controlled by the half-wave plate.

Computational Methods: Density functional theory calculations were performed using the Vienna Ab Initio Simulation Package (VASP).[69,70] The projector-augmented wave (PAW) method[71,72] was used to represent core and valence electrons; the valence electronic configurations for Sn and S are $4d^{10}5s^25p^2$ and $3s^23p^4$, respectively. Electron exchange and correlation were modeled using the PBE functional[73,74] and dispersive interactions were modeled using the Tkatchenko–Scheffler method with iterative Hirshfeld partitioning.[75,76] The kinetic-energy cutoff was set to 550 eV. A Gaussian smearing of 0.01 eV was used for Brillouin-zone integrations along with 3000 grid points for evaluating the electronic density of states. The supercell for the stacking fault model (*P*3*m*1) was constructed based on a prototypical CdI_2 structure. To minimize numerical symmetry-breaking, especially within the basal plane, the structure was relaxed using a multi-step process wherein both cell shape and atomic positions were relaxed at first with a force tolerance of 10^{-2} eV $Å^{-1}$, followed by secondary relaxation of ionic positions with a force tolerance of 10^{-3} eV $Å^{-1}$, and final symmetrization of the structure and re-relaxation with a force tolerance of 10^{-4} eV $Å^{-1}$. An $8 \times 8 \times 1$ *k*-point mesh was used for structural relaxation. The final structure was further re-symmetrized using the ASE[77] package (symmetry tolerance of 10^{-5} Å) to maintain a structure that is as close as possible to *P3m1* symmetry. The relaxed structure is provided in the SI. The difference in total energy per formula unit (f.u.) of SnS_2 between this stacking fault model and 2H SnS_2 is 0.5 meV/f.u. and all of the Γ-point phonon modes (excluding trivial translations) are positive, indicating that this structure is both thermodynamically feasible and stable. After relaxation, DFT wavefunctions were recalculated using a denser $16 \times 16 \times 2$ *k*-point mesh. Shift-current tensors were calculated using the implementation in the Wannier90 software package.[78] For these calculations, the Brillouin zone was sampled using a denser $120 \times 120 \times 15$ *k*-point mesh (interpolated) and the numerical broadening was set to 0.1 eV. The total spread of the Wannier functions was converged to under 10^{-9} $Å^2$. For the shift-current calculations, numerical tests revealed that the results were insensitive to further refinement of the interpolated *k*-point mesh. Additional details are provided in the SI.

Supporting Information

Supporting Information is available from the Wiley Online Library or from the author.

Acknowledgements

K.K., S.K., and L.V.T contributed equally to this work. The authors gratefully acknowledge funding from the US National Science Foundation DMR 1750944, NSF DMR 2202472, and NSF-BSF 2150562, and from The Gapontsev Family Collaborative Venture Fund. The authors thank Dr. G. Tompsett for help with Raman measurements. The authors thank Jim Fettinger for help with the XRD measurements.

Conflict of Interest

The authors declare no conflict of interest.

Data Availability Statement

The data that support the findings of this study are available from the corresponding author upon reasonable request.

Keywords

2D materials, shift current, SnS2, THz emission spectroscopy, THz spectroscopy

Received: January 26, 2024
Revised: March 26, 2024
Published online: April 13, 2024

[1] F. Nastos, J. E. Sipe, *Phys. Rev. B* **2006**, *74*, 035201.
[2] J. E. Sipe, A. I. Shkrebtii, *Phys. Rev. B* **2000**, *61*, 5337.
[3] M. Bieler, *IEEE J. Sel. Top. Quantum Electron.* **2008**, *14*, 458.
[4] N. Laman, M. Bieler, H. M. van Driel, *J. Appl. Phys.* **2005**, *98*, 103507.
[5] S. Priyadarshi, M. Leidinger, K. Pierz, A. M. Racu, U. Siegner, M. Bieler, P. Dawson, *Appl. Phys. Lett.* **2009**, *95*, 151110.
[6] D. Côté, N. Laman, H. M. van Driel, *Appl. Phys. Lett.* **2002**, *80*, 905.
[7] J. Pettine, P. Padmanabhan, N. Sirica, R. P. Prasankumar, A. J. Taylor, H.-T. Chen, *Light: Sci. Appl.* **2023**, *12*, 133.
[8] M. Sotome, M. Nakamura, J. Fujioka, M. Ogino, Y. Kaneko, T. Morimoto, Y. Zhang, M. Kawasaki, N. Nagaosa, Y. Tokura, *Proc. Natl. Acad. Sci. USA* **2019**, *116*, 1929.
[9] L. Braun, G. Mussler, A. Hruban, M. Konczykowski, T. Schumann, M. Wolf, M. Munzenberg, L. Perfetti, T. Kampfrath, *Nat. Commun.* **2016**, *7*, 13259.
[10] L. G. Zhu, B. Kubera, K. Fai Mak, J. Shan, *Sci. Rep.* **2015**, *5*, 10308.
[11] K. W. Kim, T. Morimoto, N. Nagaosa, *Phys. Rev. B* **2017**, *95*, 035134.
[12] S. Y. Hamh, S.-H. Park, S.-K. Jerng, J. H. Jeon, S. H. Chun, J. H. Jeon, S. J. Kahng, K. Yu, E. J. Choi, S. Kim, S.-H. Choi, N. Bansal, S. Oh, J. Park, B. W. Kho, J. S. Kim, J. S. Lee, *Appl. Phys. Lett.* **2016**, *108*, 051609.
[13] I. Nevinskas, R. Norkus, A. Geižutis, L. Kulyuk, A. Miku, K. Sushkevich, A. Krotkus, *J. Phys. D: Appl. Phys.* **2021**, *54*, 115105.
[14] Y. Huang, L. Zhu, Z. Yao, L. Zhang, C. He, Q. Zhao, J. Bai, X. Xu, *J. Phys. Chem. C* **2017**, *122*, 481.
[15] Y. Huang, L. Zhu, Q. Zhao, Y. Guo, Z. Ren, J. Bai, X. Xu, *ACS Appl. Mater. Interfaces* **2017**, *9*, 4956.
[16] N. Dhakar, S. Kumar, A. Nivedan, S. Kumar, *J. Phys. D: Appl. Phys.* **2023**, *56*, 435105.
[17] A. M. Schankler, L. Gao, A. M. Rappe, *J. Phys. Chem. Lett.* **2021**, *12*, 1244.
[18] M. Kertesz, R. Hoffmann, *J. Am. Chem. Soc.* **1984**, *106*, 3453.
[19] A. Yan, C. S. Ong, D. Y. Qiu, C. Ophus, J. Ciston, C. Merino, S. G. Louie, A. Zettl, *J. Phys. Chem. C* **2017**, *121*, 22559.
[20] L. A. Burton, A. Walsh, *J. Phys. Chem. C* **2012**, *116*, 24262.
[21] L. A. Burton, T. J. Whittles, D. Hesp, W. M. Linhart, J. M. Skelton, B. Hou, R. F. Webster, G. O'Dowd, C. Reece, D. Cherns, D. J. Fermin, T. D. Veal, V. R. Dhanak, A. Walsh, *J. Mater. Chem. A* **2016**, *4*, 1312.
[22] Y. B. Yang, J. K. Dash, A. J. Littlejohn, Y. Xiang, Y. Wang, J. Shi, L. H. Zhang, K. Kisslinger, T. M. Lu, G. C. Wang, *Cryst. Growth Des.* **2016**, *16*, 961.
[23] E. H. Wolpert, S. J. Cassidy, A. L. Goodwin, *Phys. Rev. Mater.* **2023**, *7*, 093605.
[24] Y. Huang, E. Sutter, J. T. Sadowski, M. Cotlet, O. L. A. Monti, D. A. Racke, M. R. Neupane, D. Wickramaratne, R. K. Lake, B. A. Parkinson, P. Sutter, *ACS Nano* **2014**, *8*, 10743.
[25] B. Giri, M. Masroor, T. Yan, K. Kushnir, A. D. Carl, C. Doiron, H. Zhang, Y. Zhao, A. McClelland, G. A. Tompsett, D. Wang, R. L. Grimm, L. V. Titova, P. M. Rao, *Adv. Energy Mater.* **2019**, *9*, 1901236.
[26] H. S. Song, S. L. Li, L. Gao, Y. Xu, K. Ueno, J. Tang, Y. B. Cheng, K. Tsukagoshi, *Nanoscale* **2013**, *5*, 9666.
[27] Y. Wang, L. Huang, Z. Wei, *J. Semiconduct.* **2017**, *38*, 034001.
[28] S. Wei, C. Ge, L. Zhou, S. Zhang, M. Dai, F. Gao, Y. Sun, Y. Qiu, Z. Wang, J. Zhang, P. Hu, *ACS Appl. Electron. Mater.* **2019**, *1*, 2380.
[29] C. R. Whitehouse, A. A. Balchin, *J. Cryst. Growth* **1979**, *47*, 203.
[30] Z. Ma, Z. Yao, Y. Cheng, X. Zhang, B. Guo, Y. Lyu, P. Wang, Q. Li, H. Wang, A. Nie, A. Aspuru-Guzik, *Nano Energy* **2020**, *67*, 104276.
[31] J. R. Guenter, H. R. Oswald, *Naturwissenschaften* **1968**, *55*, 177.
[32] T. Jiang, A. Ozin, *J. Mater. Chem.* **1998**, *8*, 1099.
[33] S. Jayabal, J. Wu, J. Chen, D. Geng, X. Meng, *Mater. Today Energy* **2018**, *10*, 264.
[34] Z. Lu, G. P. Neupane, G. Jia, H. Zhao, D. Qi, Y. Du, Y. Lu, *Adv. Funct. Mater.* **2020**, *30*, 2001127.
[35] B. Pałosz, W. Pałosz, S. Gierlotka, *Bulletin de minéralogie* **1986**, *109*, 143.
[36] R. S. Mitchell, Y. Fujiki, Y. Ishizawa, *Nature* **1974**, *247*, 537.
[37] R. S. Mitchell, Y. Fujiki, Y. Ishizawa, *J. Cryst. Growth* **1982**, *57*, 273.
[38] W. Mortelmans, A. Nalin Mehta, Y. Balaji, S. El Kazzi, S. Sergeant, M. Houssa, S. De Gendt, M. Heyns, C. Merckling, *2D Mater.* **2020**, *7*, 025027.
[39] A. Dewambrechies, A. Y. Polyakov, B. Küçüköz, T. O. Shegai, *J. Phys. Chem. C* **2023**, *127*, 15395.
[40] X. Lu, M. I. B. Utama, J. Lin, X. Luo, Y. Zhao, J. Zhang, S. T. Pantelides, W. Zhou, S. Y. Quek, Q. Xiong, *Adv. Mater.* **2015**, *27*, 4502.
[41] Z. Lei, Y. Huang, W. Du, Z. Fan, J. Chang, H. Wang, Y. Jin, X. Xu, *J. Phys. Chem. C* **2020**, *124*, 21559.
[42] Z. Lei, Y. Huang, Z. Fan, W. Du, C. He, H. Wang, Y. Jin, X. Xu, *Appl. Phys. Lett.* **2020**, *116*, 161901.
[43] A. M. Cook, B. M. Fregoso, F. de Juan, S. Coh, J. E. Moore, *Nat. Commun.* **2017**, *8*, 14176.
[44] L. Lutterotti, S. Matthies, H. Wenk, *CPD Newsletter* **1999**, *21*, 14.
[45] V. V. Pujar, J. D. Cawley, *J. Am. Ceram. Soc.* **1995**, *78*, 774.
[46] D. Pandey, P. Krishna, *J. Phys. D: Appl. Phys.* **1977**, *10*, 2057.
[47] N. Anitha, M. Anitha, L. Amalraj, *Optik* **2017**, *148*, 28.
[48] M. N. Amroun, M. Khadraoui, *Optik* **2019**, *184*, 16.
[49] A. J. Smith, P. E. Meek, W. Y. Liang, *J. Phys. C: Solid State Phys.* **1977**, *10*, 1321.
[50] J. M. Skelton, L. A. Burton, A. J. Jackson, F. Oba, S. C. Parker, A. Walsh, *Phys. Chem. Chem. Phys.* **2017**, *19*, 12452.
[51] D. G. Cooke, *Photocond. Photocond. Mater.* **2022**, *1*, 369.
[52] J. M. Gonzalez, I. I. Oleynik, *Phys. Rev. B* **2016**, *94*, 125433.
[53] W. Zhang, D. Turchinovich, *Opt. Express* **2021**, *29*, 24411.
[54] L. V. Titova, C. L. Pint, Q. Zhang, R. H. Hauge, J. Kono, F. A. Hegmann, *Nano Lett.* **2015**, *15*, 3267.
[55] X. Ropagnol, F. Blanchard, T. Ozaki, M. Reid, *Appl. Phys. Lett.* **2013**, *103*, 161108.
[56] E. Castro-Camus, J. Lloyd-Hughes, M. B. Johnston, *Phys. Rev. B* **2005**, *71*, 195301.
[57] M. Reid, R. Fedosejevs, *Appl. Opt.* **2005**, *44*, 149.

[58] Y. Sakai, I. Kawayama, H. Nakanishi, M. Tonouchi, *Sci. Rep.* **2015**, *5*, 13860.
[59] P. Gu, M. Tani, S. Kono, K. Sakai, X. C. Zhang, *J. Appl. Phys.* **2002**, *91*, 5533.
[60] J. Maysonnave, S. Huppert, F. Wang, S. Maero, C. Berger, W. de Heer, T. B. Norris, L. A. De Vaulchier, S. Dhillon, J. Tignon, R. Ferreira, J. Mangeney, *Nano Lett.* **2014**, *14*, 5797.
[61] P. A. Obraztsov, N. Kanda, K. Konishi, M. Kuwata-Gonokami, S. V. Garnov, A. N. Obraztsov, Y. P. Svirko, *Phys. Rev. B* **2014**, *90*, 241416.
[62] N. Laman, M. Bieler, H. M. van Driel, *J. Appl. Phys.* **2005**, *98*, 103507.
[63] S. V. Gallego, J. Etxebarria, L. Elcoro, E. S. Tasci, J. M. Perez-Mato, *Acta Crystallogr A Found Adv* **2019**, *75*, 438.
[64] M. Camarasa-Gómez, A. Ramasubramaniam, J. B. Neaton, L. Kronik, *Phys. Rev. Mater.* **2023**, *7*, 104001.
[65] A. Ramasubramaniam, D. Wing, L. Kronik, *Phys. Rev. Mater.* **2019**, *3*, 084007.
[66] Y. Shan, Y. Li, D. Huang, Q. Tong, W. Yao, W.-T. Liu, S. Wu, *Sci. Adv.* **2018**, *4*, eaat0074.
[67] E. Sutter, H.-P. Komsa, A. A. Puretzky, R. R. Unocic, P. Sutter, *ACS Nano* **2022**, *16*, 21199.
[68] G. Domingo, R. S. Itoga, C. R. Kannewurf, *Phys. Rev.* **1966**, *143*, 536.
[69] G. Kresse, J. Furthmüller, *Phys. Rev. B* **1996**, *54*, 11169.
[70] G. Kresse, J. Furthmüller, *Comput. Mater. Sci.* **1996**, *6*, 15.
[71] P. E. Blöchl, *Phys. Rev. B* **1994**, *50*, 17953.
[72] G. Kresse, D. Joubert, *Phys. Rev. B* **1999**, *59*, 1758.
[73] J. P. Perdew, K. Burke, M. Ernzerhof, *Phys. Rev. Lett.* **1997**, *78*, 1396.
[74] J. P. Perdew, K. Burke, M. Ernzerhof, *Phys. Rev. Lett.* **1996**, *77*, 3865.
[75] A. Tkatchenko, M. Scheffler, *Phys. Rev. Lett.* **2009**, *102*, 073005.
[76] T. Bučko, S. Lebègue, J. G. Ángyán, J. Hafner, *J. Chem. Phys.* **2014**, *141*.
[77] A. Hjorth Larsen, J. Jørgen Mortensen, J. Blomqvist, I. E. Castelli, R. Christensen, M. Dulak, J. Friis, M. N. Groves, B. Hammer, C. Hargus, E. D. Hermes, P. C. Jennings, P. Bjerre Jensen, J. Kermode, J. R. Kitchin, E. Leonhard Kolsbjerg, J. Kubal, K. Kaasbjerg, S. Lysgaard, J. Bergmann Maronsson, T. Maxson, T. Olsen, L. Pastewka, A. Peterson, C. Rostgaard, J. Schiøtz, O. Schütt, M. Strange, K. S. Thygesen, et al., *J. Phys.: Condens. Matter* **2017**, *29*, 273002.
[78] G. Pizzi, V. Vitale, R. Arita, S. Blügel, F. Freimuth, G. Géranton, M. Gibertini, D. Gresch, C. Johnson, T. Koretsune, J. Ibañez-Azpiroz, H. Lee, J.-M. Lihm, D. Marchand, A. Marrazzo, Y. Mokrousov, J. I. Mustafa, Y. Nohara, Y. Nomura, L. Paulatto, S. Poncé, T. Ponweiser, J. Qiao, F. Thöle, S. S. Tsirkin, M. Wierzbowska, N. Marzari, D. Vanderbilt, I. Souza, A. A. Mostofi, et al., *J. Phys.: Condens. Matter* **2020**, *32*, 165902.